IEEE Access
Multidisciplinary | Rapid Review | Open Access Journal

Received June 26, 2019, accepted July 15, 2019, date of publication July 18, 2019, date of current version August 5, 2019.

Digital Object Identifier 10.1109/ACCESS.2019.2929508

A Novel Surface-Scanning Device for Intraoperative Tumor Identification and Therapy

HAIBO WANG[1], ZHONGYUAN PING[1], YINGWEI FAN[2], HONGXIANG KANG[2], AND SIYANG ZUO[1], (Member, IEEE)

[1]Key Laboratory of Mechanism Theory and Equipment Design of Ministry of Education, Tianjin University, Tianjin 300072, China
[2]Beijing Institute of Radiation Medicine, Beijing 100850, China

Corresponding author: Siyang Zuo (siyang_zuo@tju.edu.cn)

This work was supported in part by the National Natural Science Foundation of China under Grant 61773280, in part by the Tianjin Municipal Science and Technology Department Program under Grant 16JCYBJC40700, and in part by the China Postdoctoral Science Foundation under Grant 2018M643846.

ABSTRACT Tissue identification, tumor margin identification, and therapy are major concerns for surgeons. Endomicroscopy can provide *in vivo*, *in situ* cellular-level images for the real-time assessment of tissue pathology. Hence, laser ablation can be performed in a minimally invasive manner to kill cancerous tissue while preserving normal tissue, allowing less pain and shorter recovery time. Combining endomicroscopy with laser ablation is a new area and has high potential to be a promising system. However, it is challenging to assess a surgical site using individual microscopic images due to the limited field-of-view (FoV) and difficulties associated with manually manipulating the probe. In this paper, a novel robotic device for intraoperative large-area endomicroscopy imaging and image-guided ablation is proposed, demonstrating a highly accurate and stable surface-scanning mechanism to obtain histology-level endomicroscopy mosaics. The device also includes a laser ablation fiber to precisely ablate target tissue under image guidance without the need for an additional tool. The device achieves pre-programmed scanning trajectory with a high positioning accuracy of 0.21 mm and obtains a large FoV of more than 13.9 mm^2 from a range of *ex vivo* human and animal tissue experiments. We perform *in vivo* image-guided ablation of porcine thyroid gland tissue in robotic-assisted endomicroscopy. The experimental results demonstrate that the proposed device can generate large-area, histology-level microscopic images, and ablate suspicious areas of diseased soft biological tissue, showing the potential of the device for future intelligent system and improve robotic-assisted surgery.

INDEX TERMS Minimally invasive surgery, surgical robot, image mosaicing, optical biopsy, laser ablation.

I. INTRODUCTION

Cancer is a major public health problem and it has become the leading death in most economically developed countries. It was estimated that there were approximately 14.1 million new cancer cases and 8.2 million deaths in 2012 worldwide [1]. Complete resection of the tumor is the most effective treatment to prevent cancer recurrence. However, due to inadequate imaging, incomplete tumor resection is a frequent occurrence [2]. Currently, the presence of residual tumors is confirmed by histopathological examination, which is the 'gold standard' for identifying cancerous tissue. However, this method is time consuming and depends on discrete sampling in a given region, and may not represent the true state of the target tissue. In some cases, the patient needs to return to the operating theatre for further surgery because some cancer cells remain on the edge of resected tissue [3]. The re-operation has the risk of infection, poor cosmesis and high costs. Thus, there is an increasing demand for real-time, *in situ*, high resolution imaging techniques for tissue assessment and image-guided precision therapy techniques for edge marking and tumor clearing.

In recent years, probe-based confocal laser endomicroscopy (pCLE) has become a powerful imaging tool that provides high resolution, *in situ*, *in vivo* images at cellular level [4]. Generally, the target tissue has previously

The associate editor coordinating the review of this manuscript and approving it for publication was Chaker Larabi.

been stained with topical acriflavine hydrochloride or intravenously administered fluorescein sodium [5], [6], and then an imaging fiber bundle is used to relay light from the tissue to the external optical system, avoiding tissue damage caused by pinch biopsy. Multiple studies have shown the potential applications of image morphological characteristics such as intestinal mucosa, breast cancer tissue and gastric intestinal metaplasia (GIM) [7]–[10]. In addition, endomicroscopy can also identify parathyroid tissues and differentiate malignant from unaffected lymph nodes in parathyroidectomy [11], [12].

Despite promising prospects for preliminary clinical trials, a significant limitation of endomicroscopy is that the field-of-view (FoV) is smaller than traditional frozen section biopsies. The FoV of high resolution probes is typically less than 0.5 mm (e.g., 240 μm for Cellvizio UHD Miniprobe), resulting in the analysis of only a small number of cells, making it difficult for pathologists to correctly interpret the tissue morphology. This limitation is caused by the limited number of fiber cores in the fiber bundle, and video mosaicing techniques [13], [14] can alleviate this issue by merging adjacent images together as the probe moves across the tissue surface. However, it is difficult to achieve an accurate scanning manually. In addition, the commercial available endomicroscopes are complex and extremely expensive, limiting the popularity of clinical applications, especially in low- and middle-income regions and countries. Therefore, the low-cost wide field fluorescence endomicroscopy was developed [15].

These limitations have motivated the development of robotic manipulators and hand-held smart devices to facilitate smooth and accurate scanning of the probe on tissue surface [16]–[20], preferably improving the availability and diagnostic yield of endomicroscopy. For example, Erden et al. proposed a miniature distal scanner that can perform automated spiral scanning on the liver surface [17]. S. Zuo et al. developed gear-guided linkage scanning mechanisms to achieve large area scanning of the breast cavity [18], [19]. P. Giataganas et al. proposed a robotic scanning device using two cam roller mechanism [20]. However, these devices [16]–[18], [20] lack the ability to maintain stable contact between probe and tissue. In order to obtain high quality images, the probe-tissue contact force should maintained between 0.1 N to 0.5 N [21], [22]. Excessive contact force will disturb the hemodynamics of local tissue, resulting in spectral alterations [22]. Thus, the probe needs to maintain continuous and stable contact with the tissue to obtain high quality image during scanning. However, these instruments [16]–[18], [20] lack the ability to achieve force feedback and cannot maintain stable probe-tissue contact. The robotic scanning device [19] can passively maintain consistent probe-tissue contact through a specially designed spring structure. To maintain desired probe-tissue contact force magnitude, W. T. Latt et al. proposed several mechatronic instruments that can actively adjust the axial position of the probe [23], [24]. However, these instruments [23], [24] can only maintain a stable single-point probe-tissue contact under static conditions and cannot achieve stable feedback control of the probe during scanning.

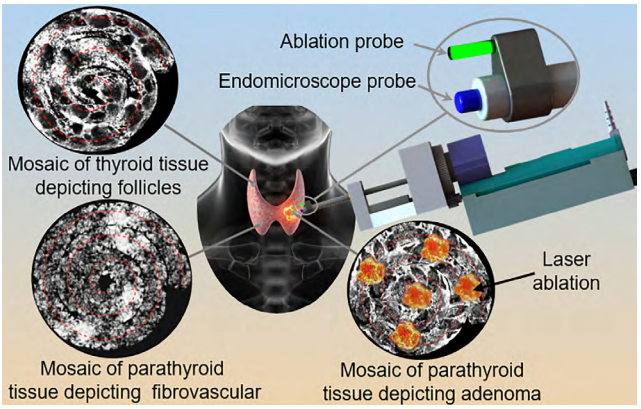

FIGURE 1. The concept of the robotic scanning device to provide large field-of-view images and image-guided laser ablation for using in thyroidectomy.

In addition, endomicroscopy can only provide real-time histological information but it cannot mark or eliminate suspicious areas and tumor margins. Laser ablation is an effective technology for eliminating cancerous tissue, and previous studies has shown that it can be used in surgical oncology [25], [26]. It utilizes the thermal effects of laser probes to damage intracellular DNA and DNA-binding structures, ultimately leading to cell death by protein denaturation [27]. However, such technology is usually guided by the surgeon's visual recognition of diseased tissues and is limited to macroscopic structures. Therefore, combining endimicroscopy with laser ablation has high potential to be a promising system that can further benefit minimally invasive surgery (MIS) by providing real-time tumor margin identification and image-guided precise therapy.

This application therefore requires a novel robotic device capable of performing accurate scanning over large areas and image-guided ablation. In this paper, we proposes such a surface-scanning device, with a view for it to be used in thyroidectomy (Fig. 1). The device can perform different scanning trajectories on the tissue surface. A low-cost wide field fluorescence endomicroscopy was used to provide diagnostic images, and an intergraded control system consisting of force sensor, Hall sensor and servomotor was used for closed-loop control of probe-tissue contact during scanning. Additionally, the energy instrument (a green laser ablation system of 532 nm in this study) was incorporated into the device for image-guided ablation and marking tumor margins.

II. METHODS AND MATERIALS

A. MECHANICAL DESIGN

The proposed device, as shown in Fig. 2, has ability to scan different trajectories by lever motion and rotation of the scanning shaft. The mechanical structure and kinematics model of the scanning mechanism are shown in Fig. 2A-B. The lever motion is driven by the linear movement of the slide block.

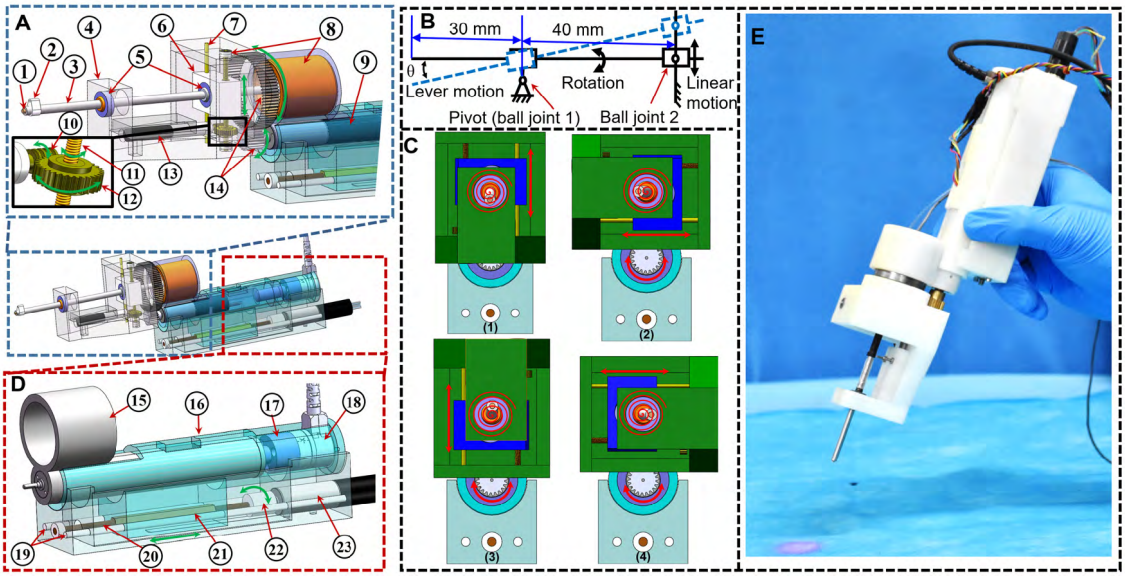

FIGURE 2. The surface-scanning device, showing (A) detailed configuration of scanning mechanism: ① fiber bundle, ② fiber fixture, ③ stainless tube, ④ outer frame, ⑤ ball joint, ⑥ slide block, ⑦ slide guide, ⑧ bearing, ⑨ motor 2, ⑩ worm, ⑪ M2 screw, ⑫ worm gear, ⑬ motor 1, ⑭ gear, (B) kinematics model of the scanning mechanism, (C) the desired spiral scanning trajectory followed by the probe, (D) detailed configuration of active linear motion mechanism: ⑮ proximal frame, ⑯ proximal slide block, ⑰ sensor fixture, ⑱ force sensor, ⑲ linear guide, ⑳ M3 screw, ㉑ nut, ㉒ coupling, ㉓ motor 3, (E) the prototype of the device.

The worm gear mechanism can convert the rotation of motor 1 (0620C012B, Faulhaber SA, Germany) into the rotation of M2 screw, and the M2 screw can drive the slide block to move smoothly along the slide guide. Two joint bearings are fixed in the outer frame and slide block, respectively, and a stainless tube passes through and is fixed in the joint bearings. Thus, motor 1 can drive the stainless tube to perform lever motion around the joint bearing 1 through the worm gear mechanism. At the same time, the stainless tube can rotate synchronously with the outer frame, which is driven by motor 2 (1226E012B, Faulhaber SA, Germany) through a pair of gears. Thus, combining lever motion with rotation, the device can perform multiple scanning trajectories, such as linear, concentric and spiral scans. In Fig. 2C, four front views of the device are given as facing the scan surface in different phase of the spiral scanning. The red line at the middle shows the desired scanning trajectory to be followed by the probe.

Another feature of the device is the force-sensitive linear servo mechanism that can maintain stable probe-tissue contact during scanning. Fig. 2D shows the mechanical components of the linear servo mechanism. The force sensor (NANO-17 SI 12/0.12, ATI Industrial Automation Corp., America) is integrated into the device to measure probe-tissue contact force. An M3 screw is connected with motor 3 (1226E012B, Faulhaber SA, Germany) by a coupling, and the nut is inserted into the proximal slide block. Thus, the motor 3 can drive the proximal slide block to axially adjust the tip position of the device. A closed-loop control algorithm of linear servo mechanism is used to maintain stable probe-tissue contact force, as detailed in Section 3.

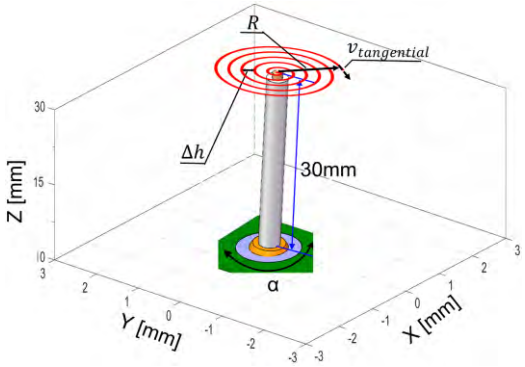

FIGURE 3. The spiral scanning trajectory of the scanning tip.

The proposed prototype is shown in Fig. 2E. The scanning shaft is 3 mm in outer diameter and 70 mm in length, incorporating a central hollow channel (2 mm in inner diameter) for passing through the imaging fiber bundle. The total length of the device including the scanning shaft is 250 mm and the total weight is 330 g.

B. KINEMATIC ANALYSIS AND SCANNING TRAJECTORY

For the proposed device, different scanning trajectories can be performed by imputing corresponding commands to the motors. We select a spiral path as an effective way to cover a circular scan area, as shown in Fig. 3.

For spiral scanning, the tangential velocity $v_{tangential}$ and loop spacing Δh are two important parameters, which can be expressed as:

$$R = \frac{30}{40} \times \frac{W_{m1}}{\mu_1} \times P_1 \times t \tag{1}$$

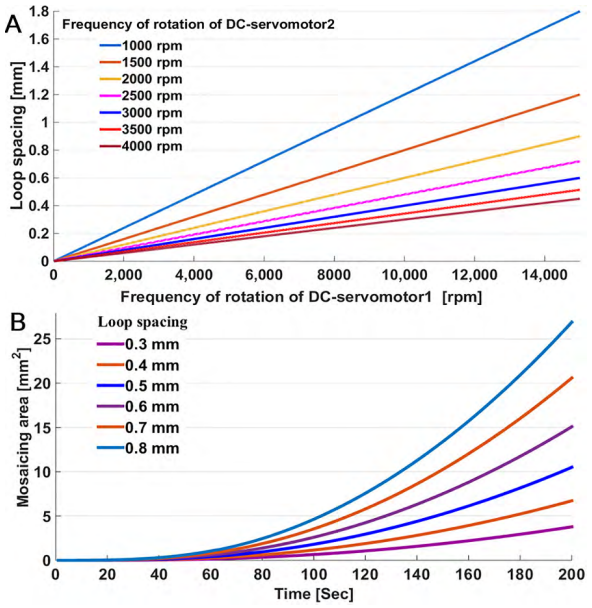

FIGURE 4. The kinematic analysis of the device, showing (A) the relationship among the loop spacing and the frequencies of rotation of motors, (B) the relationship among mosaicing area, time and loop spacing.

$$\Delta h = \frac{R \times \mu_2}{w_{m2} \times t} \tag{2}$$

$$v_{tangential} = \frac{R \times W_{m2} \times 2\pi}{\mu_2} \tag{3}$$

where R is the radius of spiral scanning trajectory. W_{m1}, μ_1 and W_{m2}, μ_2 are the frequencies of rotation and gear reduction ratio of motor 1 and motor 2, respectively. P_1 (0.4 mm) is the pitch determined by M2 screw. The distance between the joint bearings is 40 mm, and the distance from the probe to the distal joint bearing 1 is 30 mm as shown in Fig. 2B. The relationship among the loop spacing and the rotational frequencies of motors is illustrated in Fig. 4A, where W_{m1} is changed from 1000 rpm to 4000 rpm in steps of 500 rpm.

Note that the endomicroscopy used in this study is able to observe a region with a diameter of 0.8 mm, so a gapless mosaic can be obtained if the spiral scanning trajectory has a loop spacing of less than 0.8 mm. Theoretically, the gapless mosaicing area S achieved by the device can be expressed as follows:

$$\alpha = \frac{W_{m2} \times 2\pi}{\mu_2} \times t \tag{4}$$

When,

$$\frac{W_{m2} \times t}{\mu_2 \cdot 60} \leq 1$$

$$S = \int_0^{\alpha} \frac{\alpha^2}{2} d\alpha = \int_0^{t} \frac{30^2 \times W_{m1}^2 \times W_{m2} \times \pi \times P_1^2 \times t^2}{40^2 \times \mu_1^2 \times \mu_2} dt \tag{5}$$

When,

$$\frac{W_{m2} \times t}{\mu_2 \cdot 60} \geq 1$$

$$S = \int_{\alpha-2\pi}^{\alpha} \frac{\alpha^2}{2} d\alpha = \int_{t-\frac{\mu_2 \cdot 60}{w_{m2}}}^{t} \frac{30^2 \times W_{m1}^2 \times W_{m2} \times \pi \times P_1^2 \times t^2}{40^2 \times \mu_1^2 \times \mu_2} dt \tag{6}$$

Thus, the expression for the mosaicing area S can be expressed as (7).

$$S = \begin{cases} \int_0^{t} \frac{30^2 \times W_{m1}^2 \times W_{m2} \times \pi \times P_1^2 \times t^2}{40^2 \times \mu_1^2 \times \mu_2} dt & \frac{W_{m2} \times t}{\mu_2} \leq 1 \\ \int_{t-\frac{\mu_2}{W_{m2}}}^{t} \frac{30^2 \times W_{m1}^2 \times W_{m2} \times \pi \times P_1^2 \times t^2}{40^2 \times \mu_1^2 \times \mu_2} dt & \frac{W_{m2} \times t}{\mu_2} \geq 1 \end{cases} \tag{7}$$

where α is the rotation angle of the probe. The relationship among mosaicing area, time and loop spacing is shown in Fig. 4B, where W_{m2} is set to a constant rotational frequency of 500 rpm, and loop spacing is changed from 0.3 mm to 0.8 mm in steps of 0.1 mm.

C. ACTUATION AND CLOSED-LOOP FORCE CONTROL SYSTEM

All actuation is driven by three high-resolution brushless DC Servomotors (0620C012B and 1226E012B, Faulhaber, Germany) with integrated 879:1 reduction gearbox (Faulhaber, Germany) for two of them, and 256:1 for the remainder. An integrated magnetic encoding system (analogue Hall sensors (K1855 and K2280, Faulhaber, Germany)) and three dedicated motor controllers (MCBL 3002 S CF, Faulhaber, Germany) are used for closed-loop position control of servomotors. The motor controllers' embedded software communicates with the control system via a CAN bus with a 1000 kbps Baud rate. A termination resistor of 120 Ω is used to reduce reflections of the signal on the CAN bus caused by the use of multiple motors. A USB-to-CAN interface (IXXAT, HMS Industrial Networks, Germany) connects the CAN bus to the control system. All components are powered by a 12 V power supply. A custom user interface has been developed in Labview (National Instruments Corp., America) for controlling the device from a standard PC. Once the scan parameters are entered, the device automatically scan the tissue surface.

The performance of the scanning device is closely related the motor control. Fig. 5A shows the closed-loop control diagram of the lever motion. θ_t is the target bending angle and θ_f is the current bending angle. x is the differential linear displacement calculated from the slide block's target position x_t and current position feedback x_f. V is the corresponding output analog voltage generated by motion controller for

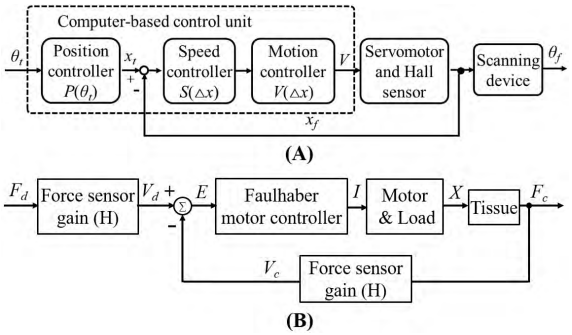

FIGURE 5. The overview of the control system, showing (A) the control diagram for precise motor control, (B) the closed-loop force control system.

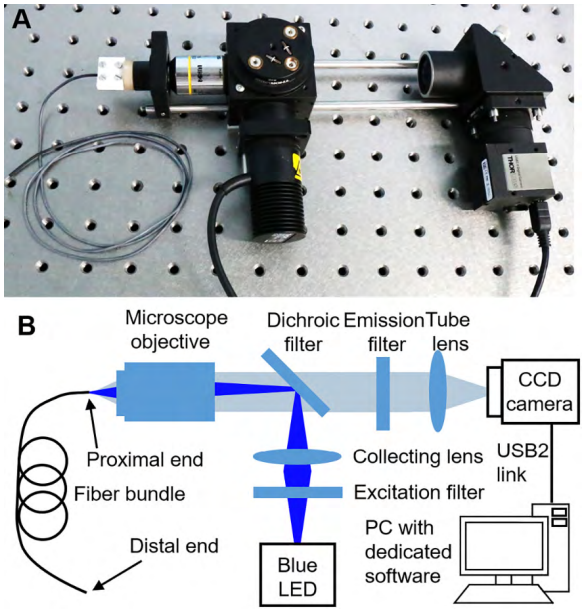

FIGURE 6. The low-cost wide field fluorescence endomicroscopy, showing (A) the prototype of the endomicroscopy, (B) the schematic of endmicroscopy.

precise motor control. The independent control process of the rotation is the same as the lever motion.

The block diagram of the closed-loop force control system for maintaining stable probe-tissue contact is shown Fig. 5B. The current probe-tissue contact force F_c is measured by the force sensor (NANO-17 SI 12/0.12, ATI Industrial Automation Corp., America), and acquired by a multifunction DAQ device (USB6210, National Instruments Corp., America). F_d is the desired contact force. The error E between the measured voltage V_c and the desired voltage V_d is used as an input to closed-loop control scheme in the motor controller (MCBL 3002 S CF, Faulhaber, Germany). The Faulhaber motor controller then outputs corresponding analog voltage I based on the voltage level received at its input for precise motor rotation.

D. OPTICAL SYSTEM AND MOSAICING SOFTWARE

The optical system, as shown in Fig. 6A, is a low-cost wide field fluorescence endomicroscopy coupled to a leached fiber bundle (SCHOTT North America. Inc, America). The bundle is 895 mm in length and has a maximum diameter of 1.27 mm, and contains 18,000 fiber cores. Fig. 6B shows the schematic of the endmicroscopy. The source of illumination is a 455 nm blue LED. The 450 nm excitation filter and collecting lens focus the light on the dichroic filter and image onto a microscope objective. The beam is then focused at the proximal end of the fiber bundle and transfers to the distal face. When the probe is in contact with the stained tissue, the fluorescent emission returns along the optical path and produces an image on the CCD camera. Then, the CCD camera records and stores the image at 15 frames per second (FPS).

For image mosaicing, we used offline algorithms described previously [28], [29]. The offline algorithms can obtain more satisfactory mosaics and can store, process and focus on images of suspicious areas. A Gaussian filter is applied to remove the honeycomb-like structure arising from the discrete fiber cores, and a circular window is adopted to remove the irregular edges of the FoV. Then, the normalized cross correlation (NCC) is used to estimate the most likely rotation angle and lateral shift between each rotated image and the previous frame, and then the frame is added to the mosaic at the estimated position.

III. RESULTS

A. MECHANICAL PERFORMANCE ECALUATION

In order to evaluate the mechanical performance of the device, a mini gyro sensor (JY61P, WitMotion Shenzhen Co.,Ltd, China) with swing angle accuracy of 0.05° was used to verify the lever motion and rotation characteristics. The experimental setup is shown in Fig. 7A. The device was fixed on the workbench, and the mini gyro sensor was fixed at the distal end of the device to measure the swing angle of lever motion and the rotation angle.

Five repeatability measurements were performed to evaluate the lever motion and rotation performance. For lever motion, measurements were performed in two parts: (i) the scanning shaft was controlled to swing from center to end and then return to center, (ii) from center to anther end and finally return to center. The distal end position P_{tip} can be calculated by follow equation:

$$P_{tip} = 30 \times \theta \tag{8}$$

where θ is the swing angle. The relationship among the target position, actual distal end position, and repeatability error is shown in Fig. 7B.

We also tested the rotation performance in detail. The scanning shaft was controlled to rotate from 0° to 360° (iii), and then return to 0° (iv). The distal end position P_{tip} can be calculated by follow equation:

$$P_{tip} = R \times \alpha \tag{9}$$

where R is the radius of spiral scanning trajectory, and α is the rotation angle. The relationship among the target angle, measured angle and repeatability error is shown in Fig. 7C.

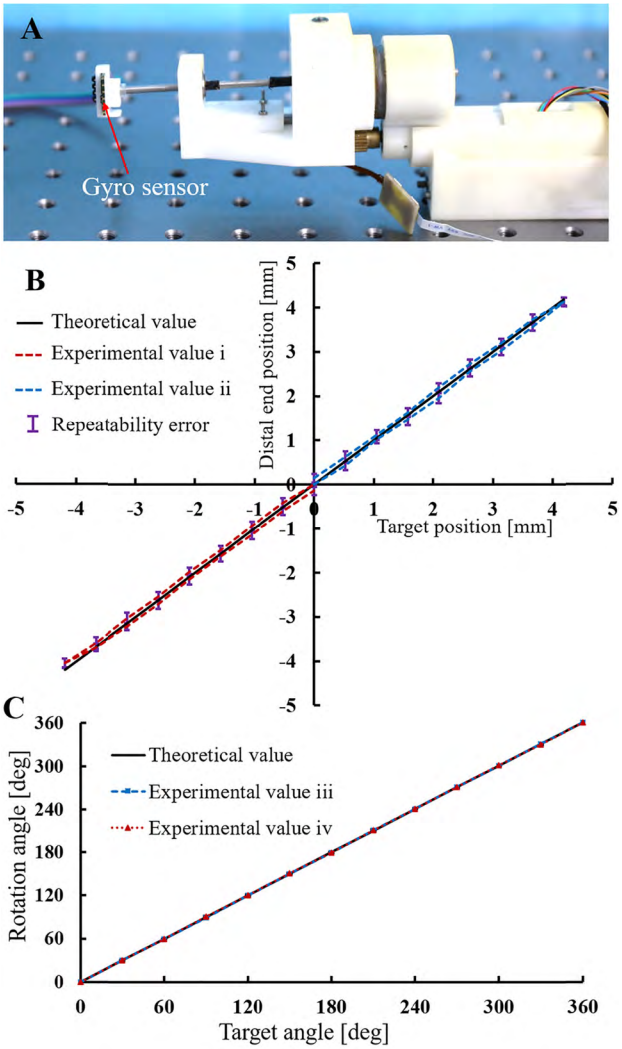

FIGURE 7. Mechanical performance evaluation of the device, showing (A) the experiment setup, (B) mechanical result of lever motion, (C) mechanical result of rotation.

We also measured the forces generated by the scanning shaft using a digital force gauge. The motion range, repeatability error, tip positioning accuracy and minimum generated force are shown in Table 1.

B. TRAJECTORY PERFORMANCE EVALUATION

In order to evaluate the scanning trajectory of the device, detailed laboratory experiments were performed. An Electromagnetic Tracking system (Aurora, NDI Corp., America) was used to record the tip position. The experimental setup is shown in Fig. 8A, the device was clamped at the workbench, and an Aurora micro sensor (part number: 610059, dimensions: 0.8 mm diameter and 9 mm length) was inserted into the channel of the scanning shaft.

In this experiment, the device was controlled to perform spiral trajectories with different loop spacings. We performed each scanning five times, and randomly chose one set of data to evaluate the trajectory. The experiment results are shown

TABLE 1. The characteristics of the lever motion and rotation.

Measurement item	(i)	(ii)	(iii)	(iv)
Range (°)	0 to 8	0 to -8	0 to 360	360 to 0
Repeatability error (°)	0.4±0.1	0.4±0.1	0.2±0.1	0.2±0.1
Tip positioning accuracy (mm)	0.21±0.05	0.21±0.05	≤0.015	≤0.015
Minimum generated force (N)	1.5	1.5	1.2	1.2

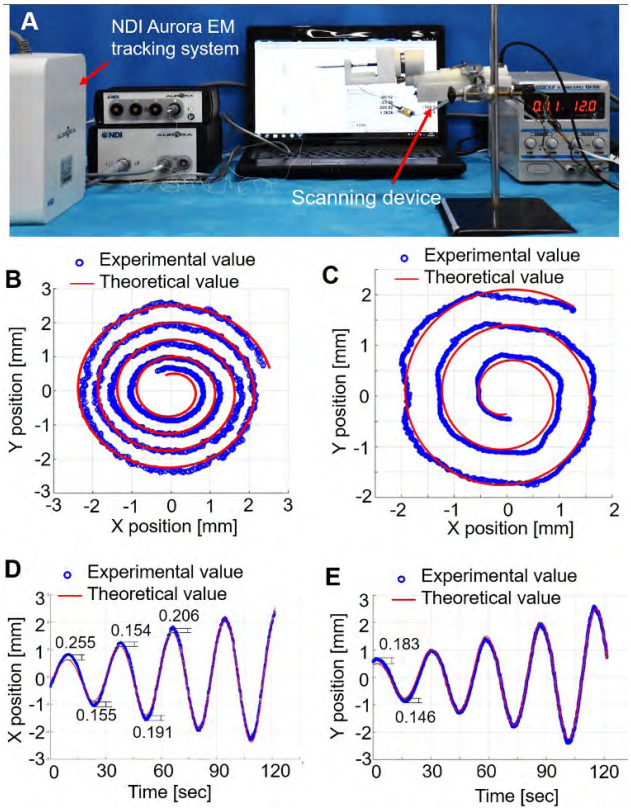

FIGURE 8. Trajectory performance evaluation of robotic scanning device, showing (A) the experiment setup, (B) spiral trajectory of 0.5 mm loop spacing, (C) spiral trajectory of 0.7 mm loop spacing, (D) X position, (E) Y position.

in Fig. 8B-E. Fig. 8B-C shows the spiral scanning trajectories with loop spacing of 0.5 and 0.7 mm, respectively. Fig. 8D-E shows the target and actual x and y position of spiral scanning trajectory (0.5mm in the loop spacing).

C. FORCE CONTROL PERFORMANCE

Since the force sensor is placed at the proximal end of the device, the measured force is a combination of the probe-tissue contact force and the internal friction of device. Accurate calculation of friction force is required to maintain stable probe-tissue contact. Thus, a series of bench experiments were conducted to evaluate the force control performance. The experimental setup is shown in Fig. 9A. The device was fixed at the workbench, and the simulated soft tissue (a piece of foam) was attached to the external force

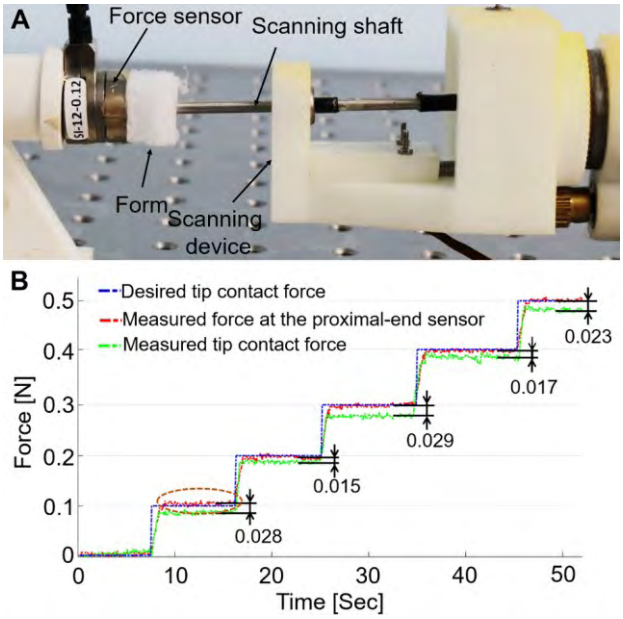

FIGURE 9. Force control performance of the device, showing (A) the experiment setup, (B) comparison of the contact force at the tip of the instrument and the force measured at the proximal-end force sensor.

sensor (NANO-17 SI 12/0.12, ATI Industrial Automation Corp., America), and then the scanning shaft was controlled to perpendicular contact with the simulated soft tissue. Thus, the actual tip contact force can be directly measured by the external force sensor, and the internal friction can be calculated by subtracting the forces measured by the external and proximal-end force sensors. Then, the internal friction is pre-calculated in the closed loop force control algorithm, and the desired tip contact force is gradually increased from 0 N to 0.5N in steps of 0.1N. The desired tip contact force, the force measured at the proximal-end force sensor and the measured tip contact force at the external force sensor are shown in Fig. 9.

We found experimentally that the contact force of 0.1N was necessary to ensure consistent results. The dotted circle shows the settings chosen for the experimental results in the following section.

D. LENS TISSUE PAPER AND PORCINE TISSUE EXPERIMENTS

In order to evaluate the scanning and mosaicing performance of the device, we firstly performed scanning experiments on a piece of lens tissue paper. The experimental setup is shown in Fig. 10A. The device was fixed at a passive arm, and the tissue paper was previously stained with acriflavine (0.01% w/v in PBS, excitation wavelength: 430 nm, emission wavelength: 512 nm). In this experiment, the device was controlled to maintain a constant loop spacing of 0.3 mm. We performed four spiral scans and randomly chose two sets of data for mosaicing evaluation. The mosaicing results are shown in Fig. 10B-C, which cover an area of approximately 7.97 mm^2 and 9.13 mm^2, respectively. The intended scanning

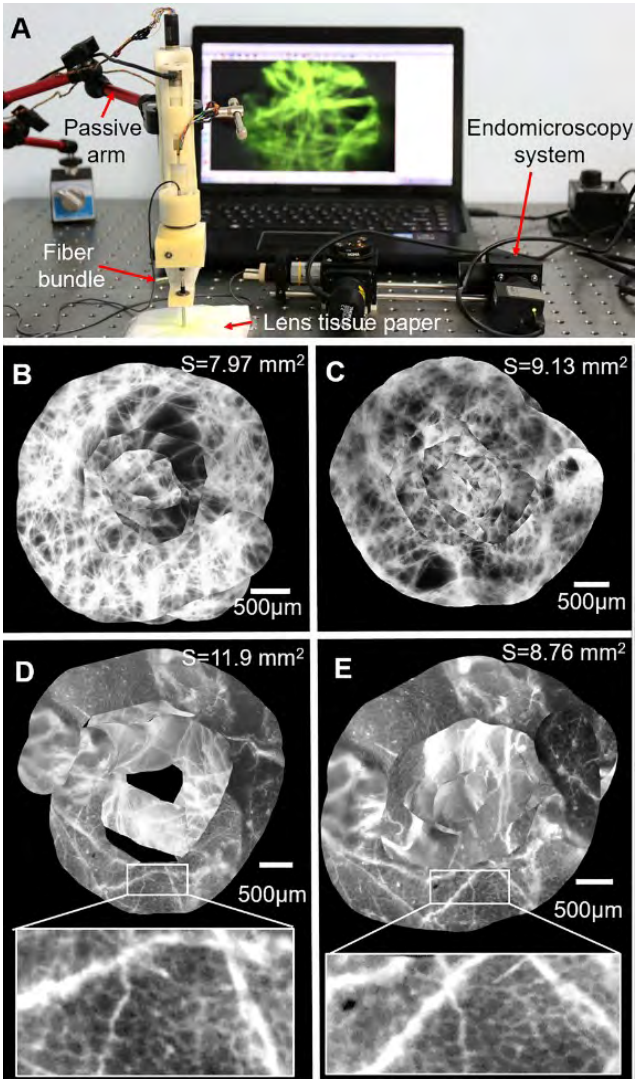

FIGURE 10. The mosaicing performance evaluation of the system, showing (A) the experiment setup for bench experiment with lens tissue paper, (B-C) the mosaics of lens tissue paper, (D-E) the mosaics of porcine belly tissue.

areas are 9.83 mm^2 and 11.56 mm^2. Thus, the ratio of the coverage area to the intended area are 0.81 and 0.79, respectively. The results demonstrate that the device can obtain gapless mosaics, and the fiber structures of the lens tissue paper can be clearly observed.

In order to evaluate the mosaicing performance of the device on soft tissue, a series of experiments were performed on a piece of porcine belly tissue. In this experiment, we performed spiral scans with loop spacing of 0.7 mm and 0.4 mm. We performed each scans six times. However, due to the tissue deformation, we failed to obtain satisfactory mosaics several times. We selected two acceptable mosaics from the mosaicing results, as shown in Fig. 10D-E. Fig. 10D shows a mosaic with loop spacing of 0.7 mm, covering an area of approximately 11.9 mm^2 and the ratio of the coverage area to the intended area (17.4 mm^2) is 0.68. Fig. 10E shows a second scan with loop spacing of 0.4 mm, covering an area

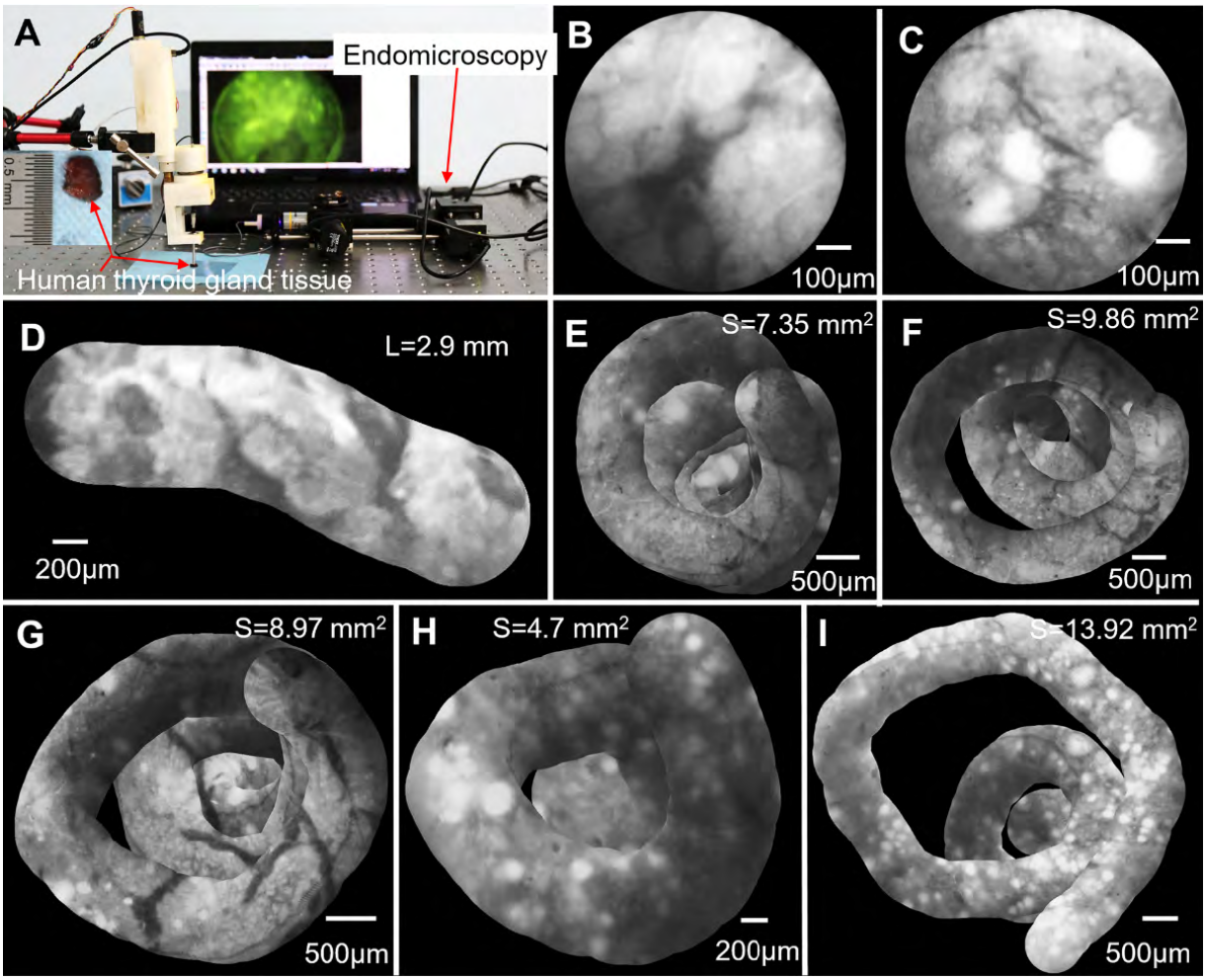

FIGURE 11. The *ex vivo* human thyroid gland tissue experiments, showing (A) the experiment setup, (B-C) the imaging performance of the endomicroscopy system, (E-I) the mosaicing results of *ex vivo* human thyroid gland tissue.

of approximately 8.76 mm^2 (0.72 in ratio). We observed that small gaps were existed in the mosaic, as shown in Fig. 10D. The main cause for the gap is the deformation of porcine belly tissue during the scanning. However, the key morphological features such as the adipocytes, the large polygonal-shaped fat cells and fibrous tissue can be clearly identified from the mosaics, allowing for a global appreciation of the tissue morphology.

E. EX VIVO HUMAN THYROID GLAND TISSUE EXPERIMENTS

In order to evaluate the ability of the device to obtain consistent images on human thyroid gland tissue, an acriflavine-stained *ex vivo* human thyroid gland tissue was used for experiments. Ethics approval was obtained through Tianjin Medical University General Hospital. The experimental setup is shown in Fig. 11A. The device was attached to a passive arm and the thyroid gland tissue was placed on a plastic-sterilized slide. Only a small portion of normal thyroid gland tissue was available (approx. 8 × 6 mm). Firstly, we verified the imaging performance of the wide field fluorescence endomicroscopy by adjusting the probe into close contact with the tissue. The images of thyroid gland tissue are shown in Fig. 11B-C. The key morphological features of thyroid gland can be identified from these images.

Then, we conducted experiments to evaluate the mosaicing performance of the device. In this experiments, the device was controlled to perform linear and spiral scans, and the loop spacing of spiral trajectory was controlled to be 0.4 mm. One linear and five spiral scans were selected for mosaicing evaluation, as shown in Fig. 11D-I. Fig. 11D shows a mosaic of linear scanning of approximately 2.9 mm in length. Fig. 11E-I show the mosaics of spiral scanning, covering an area of approximately 7.35 mm^2, 9.86 mm^2, 8.97 mm^2, 4.7 mm^2 and 13.92 mm^2, respectively. The ratio of coverage area to expected area are 0.69 (Fig. 11E), 0.75 (Fig. 11F), 0.73 (Fig. 11G), 0.71 (Fig. 11H) and 0.68 (Fig. 11I). Due to the tissue deformation of soft tissue and irregular thyroid surface, there are unexpected overlaps and small gaps in these mosaics.

F. IN VIVO VALIDATION WITH SWINE EXPERIMENTS

The device integrated with the laser ablation system was evaluated *in vivo* on a male swine weighing approximately

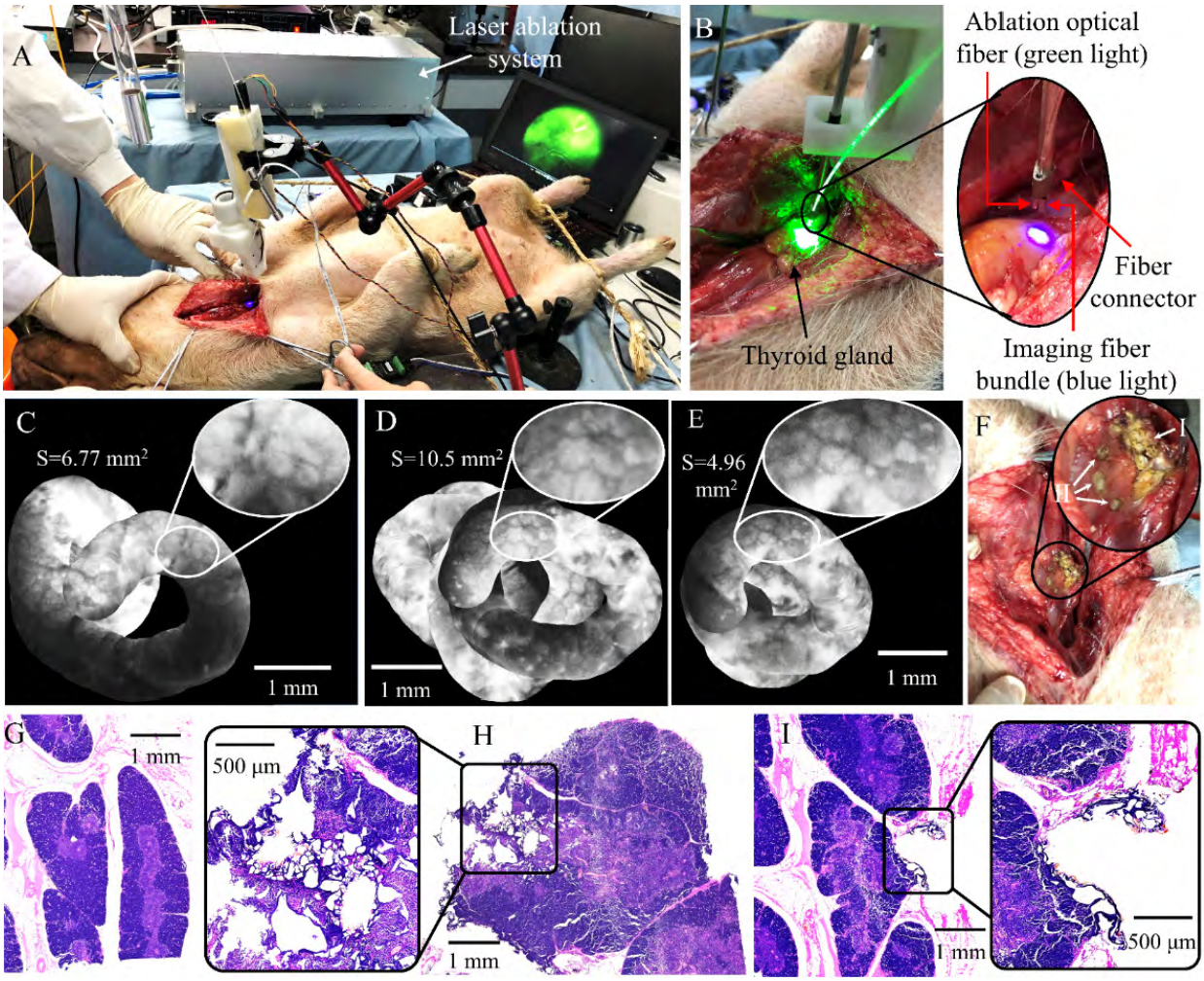

FIGURE 12. *In vivo* **experiments with swine, showing (A-B) the experiment setup, (C-E) mosaics of the porcine thyroid gland tissue, (F) the ablation results of the porcine thyroid gland tissue, (G) histologic image of normal porcine thyroid gland tissue, (H) histologic images of thyroid gland tissue after straight line ablation. (I) histologic images of thyroid gland tissue after single-point ablation.**

20-25 kg. Animal experiments with swine were performed in accordance with the Beijing Institute of Radiation Medicine Experiment Animal Center-approved animal protocols. The laser ablation system (wavelength: 532 nm, output power: 20 mW∼ 200 W) is developed by Beijing Institute of Radiation Medicine. The experimental setup is shown in Fig. 12A, the device was attached to a passive arm and the swine was fixed on the workbench. Before the experiments, the swine was anesthetized by intramuscular injection of 3% sodium pentobarbital solution. Conventional surgery was performed for finding the thyroid gland. Then, we performed spiral scans (loop spacing of 0.4mm) on the porcine thyroid gland surface. The thyroid gland was previously stained with acriflavine, and can be clearly distinguished from the neck anatomy as shown in Fig. 12B. We performed scans six times and extracted three sets of mosaics from these experiments as shown in Fig. 12C-E. Fig.12C shows a mosaic that covers an area of approximately 6.77 mm^2, and the ratio of the coverage area to intended area (11.47 mm^2) is 0.59. Fig.12D shows a second scan, covering an area of approximately 10.5 mm^2 (an area ratio of 0.62). Although the path did not follow the ideal spiral, the abrupt movements still collects some images from the target tissue. Fig.12E shows a satisfactory mosaic without any significant gap, covering an area of 4.96 mm^2 and the ratio of the coverage area to expected area (6.12 mm^2) is 0.81. We observed that blurred images existed in the mosaics. This is mainly caused by the tissue deformation of thyroid gland and adhesion of the thyroid mucosal tissue to the probe during scanning. In addition, the swine was not completely anesthetized, the breathing and neck movement also affected the mosaicing results. Nevertheless, the morphological characteristics of the thyroid gland tissue can be identified, and the creation of the large-area mosaics enables global appreciation of the thyroid gland tissue.

Then, we performed image-guided laser ablation on the thyroid surface. A specially designed mechanical component was used to connect ablation optical fiber (0.75 mm in diameter) with the imaging fiber bundle as shown in Fig. 12B. Since the two fibers are transversely offset by 2 mm, a complimentary offset was applied to the position of the ablation fiber to

accurately ablate at the center of the endomicrocopy image. The ablating result is shown in Fig. 12F, linear ablation (I) and single point ablation (II). During linear laser ablation (current 10 A, power 30 W), we attempted to remove part of the thyroid gland tissue, but the swine struggled vigorously due to pain, resulting in the ablation result to deviate significantly from the theoretical expectation. In single point laser ablation (current 10 A, power 30 W and duration 1 s), ablation is performed at three designated locations of the thyroid gland.

To verify the effects of laser ablation, we performed standard histological analysis of the ablated and non-ablated tissues. Fig.12G shows the histological images of normal porcine thyroid gland tissue. Fig. 12H-I shows the histological images of ablated thyroid gland tissue. Based on the data provided by this preliminary experiment, image-guided laser thermal ablation can be considered as a clinically effective, well-tolerated and safe minimally invasive technique for the surgical therapy of thyroid lesions.

IV. DISCUSSION

In this paper, we demonstrated a novel surface-scanning device for intraoperative diagnosis and therapy of diseased soft biological tissue in MIS. The key novelties of this work include: 1) the mechanical design and precise motor control enables the device to scan different trajectories, 2) the active linear actuation mechanism contributes to maintain stable probe–tissue contact during scanning, 3) image-guided laser ablation can accurately mark and ablate target areas and margins, 4) a low-cost wide field endomicroscopy for intraoperative, real-time *in vivo* imaging. By using the device, we achieved large mosaics of up to 13.92 mm^2. Compared to previous studies [17], [20] that generated mosaics of less than 3 mm^2, our device has a significant increase in area coverage. Although the device is designed in a thyroid set-up, the length of the scanning shaft can be adjusted for other surgical procedures, such as laparoscopic surgery, breast conserving surgery and eye surgery.

The results of mechanical performance indicate that the device has ability to perform lever motion and rotation with high accuracy, and the tip positioning accuracy is as high as 0.21 mm. Note that the FoV captured by the endomicroscopy is 0.8 mm in diameter, so the loop spacing for achieving gapless mosaics should be 0.8 mm or less, and the accuracy of 0.21 mm is satisfactory. The trajectory performance evaluation results show that the device can perform smooth spiral trajectories with different loop spacing. However, small errors (less than 0.255 mm) between the experimental value and theoretical value can be observed from the results, as shown in Fig. 8B-E. This is mainly caused by the backlash of the scanning mechanism, the vibration of the scanning shaft and the noise of electromagnetic tracking system.

Experimental results of force control performance indicate that closed-loop force control system is useful for maintaining stable contact between probe and tissue. Inaccuracies in the force measurement may be introduced due to friction of the mechanism. However, the purpose of the device is not to provide the operator with an accurate force measurement, but to maintain a relatively constant probe-tissue contact force during image acquiring. The friction force inside the device is not a constant value, which varies from 0.058 N to 0.248 N and is related to the device's holing position. The minimum friction occurs when the device is placed vertically, and the maximum friction occurs when it is placed horizontally. When the device is held in a constant position, the change in the magnitude of the friction was in the range of a few tens millinewtons. Due to the fluctuation of the friction, it is difficult to maintain a precise and stable probe-tissue contact as desired below 0.1 N during scanning. In general, the closed-loop control of the linear actuation structure is an effective way to maintain an acceptable level of probe–tissue contact.

The optical system used in this study is a customized low-cost wide field endomicroscopy. The overall price of the optical system, including the fiber bundle, is under $6500 far below the commercial laser confocal endomicroscopy system (Cellvizio, Mauna Kea Technologies, France) that costs over $400,000. The high flexibility of the fiber bundle can meet the requirements of small space and complex curved surgical channels. The FoV is another feature of the fiber bundle, which is approximately 800μm in diameter after removing the edge portion of the image and is larger than commercial probe (e.g. 240μm for Miniprobe, Mauna Kea Technologies, France). The limitation of the probe is the low resolution (8 μm), depending on the core spacing of the fiber bundle. However, the morphological characteristics of the target tissues can be clearly distinguished, as shown in Figs. 10-12. In addition, the optical system is simple and easy to carry.

The simple algorithms based on NCC were used for imaging mosaicing. Since the position and rotation angle of each frame are determined by comparing it with the previous frame, this method accumulates errors. Eventually, the mosaicing results are inconsistent with the theoretical expectations as shown in Figs. 10-12. More successful mosaics can be obtained by applying more complex algorithms that considers cumulative errors and tissue deformation [13].

Experimental results of lens tissue paper indicate that the device can perform stable scans according to the expected trajectory and obtain satisfactory mosaics, as shown in Fig. 10B-C. However, unexpected distortion and small gaps were observed in the mosaics of soft tissue, as shown in Fig. 10-12. The main reason is that the soft tissue is more adhesive than lens tissue paper and is more prone to tissue deformation. Especially, the highly undulating surface of soft tissue, which results in the mosaicing results to be different from intended trajectories. Actually, the tissue deformation is inevitable, and any contact-based imaging method will result in tissue deformation. Nevertheless, the proposed device can facilitate smooth and consistent movement of the probe and obtain large area mosaics at an acceptable level. In addition, some other techniques, such as 3D visualization and navigation to track probe's position [30]–[32] and visual

servoing [33] can also contribute to obtain more successful mosaic, which requires further research.

The experimental results of *in vivo* porcine thyroid gland indicate the interventional capabilities of the proposed device for providing real-time endomicroscopic images and ablation of target areas without separate tools. However, the quality of images maybe not good enough to be correlated with histological images. This is mainly due to out-of-focus background blur of the optical system. Moreover, in some cases, the pathological images show morphological features of the cross section of the thyroid gland tissue rather than surface histological analysis. Nevertheless, key morphological features of the thyroid gland tissue can be observed from the endomicroscopic images, and the creation of the large-area mosaics enables global appreciation of the target tissue. In addition, the endomicroscopy can obtain intraoperative real-time images as along as the probe is in contact with the stained tissue, while the waiting time for traditional Hematoxylin and Eosin (H&E) staining of Frozen sections is up 40 min. Furthermore, the optical system can be changed to pCLE [11], [12] for providing higher resolution images that appear more similar to conventional histological images. Other imaging techniques widely used for thyroidectomy, such as hyperspectral imaging (HSI) [34] and indocyanine green (ICG) fluorescence [35], can also be combined with the device to provide real-time histological information for diagnosis and image-guided ablation.

V. CONCLUSION

In this paper, we have developed a novel robotic surface-scanning device with force feedback for endomicroscopy in MIS. We have shown that the device can perform smooth and consistent scanning and provide a large FoV for 'optical biopsy'. In evaluation of lens tissue paper, *ex vivo* porcine belly tissue, *ex vivo* human thyroid gland tissue and *in vivo* porcine thyroid gland tissue, the device enables large area imaging and image-guided ablation. The results demonstrate the potential clinical value of the device for intraoperative *in situ* tumor margin evaluation and precise therapy.

DISCLOSURES

The authors have declared that no competing interest exists.

ACKNOWLEDGMENT

The authors would like to thank Prof. Xianghui He from Tianjin Medical University General Hospital for assistance with tissue preparation, Wei Chang and Chengquan Hu from Tsinghua University for assistance in animal experiments.

REFERENCES

[1] L. A. Torreetal, "Global cancer statistics, 2012," *CA, Cancer J. Clinicians*, vol. 65, no. 2, pp. 87–108, Mar. 2015.

[2] M. A. Kouvaraki, S. E. Shapiro, B. D. Fornage, B. S. Edeiken-Monro, S. I. Sherman, R. Vassilopoulou-Sellin, J. E. Lee, and D. B. Evans, "Role of preoperative ultrasonography in the surgical management of patients with thyroid cancer," *Surgery*, vol. 134, no. 6, pp. 946–954, Dec. 2003.

[3] S. E. Singletary, "Surgical margins in patients with early-stage breast cancer treated with breast conservation therapy," *Amer. J. Surg.*, vol. 18, no. 5, pp. 383–393, Nov. 2002.

[4] S. Zuo and G.-Z. Yang, "Endomicroscopy for computer and robot assisted intervention," *IEEE Rev. Biomed. Eng.*, vol. 10, pp. 12–25, 2017.

[5] C. Q. Li, T. Yu, X. L. Zuo, X. J. Xie, W. B. Li, C. L. Chu, F. Zuo, and Y. Q. Li,"Effects on confocal laser endomicroscopy image quality by different acriflavine concentrations," *J. Interventional Gastroenterol.*, vol. 1, no. 2, pp. 59–63, Apr. 2011.

[6] K. Nonakaet, K. Ohata, S. Ban, S. Ichihara, R. Takasugi, Y. Minato, T. Tashima, Y. Matsuyama, M. Takita, N. Matsuhashi, and H. Neumann, "Histopathological confirmation of similar intramucosal distribution of fluorescein in both intravenous administration and local mucosal application for probe-based confocal laser endomicroscopy of the normal stomach," *World J. Clin. Cases*, vol. 3, no. 12, pp. 993–999, Dec. 2015.

[7] J. M. Jabbour, M. A. Saldua, J. N. Bixler, and K. C. Maitland, "Confocal endomicroscopy: Instrumentation and medical applications," *Ann. Biomed. Eng.*, vol. 40, no. 2, pp. 378–397, Feb. 2012.

[8] R. C. Newton, D. P. Noonan, V. Vitiello, J. Clark, C. J. Payne, J. Shang, M. Sodergren, A. Darzi, and G.-Z. Yang, "Robot-assisted transvaginal peritoneoscopy using confocal endomicroscopy: A feasibility study in a porcine model," *Surgical Endoscopy*, vol. 26, no. 9, pp. 2532–2540, Sep. 2012.

[9] S. Zuo, M. Hughes, P. Giataganas, C. Seneci, T. P. Chang, and G. Yang, "Development of a large area scanner for intraoperative breast endomicroscopy," in *Proc. IEEE Int. Conf. Robot. Automat. (ICRA)*, Sep. 2014, pp. 3524–3530.

[10] L. G. Lim, K. G. Yeoh, S. Srivastava, Y. H. Chan, M. Teh, and K. Y. Ho, "Comparison of probe-based confocal endomicroscopy with virtual chromoendoscopy and white-light endoscopy for diagnosis of gastric intestinal metaplasia," *Surgical Endoscopy*, vol. 27, no. 12, pp. 4649–4655, Dec. 2013.

[11] M. Kraft, C. S. Betz, A. Leunig, and C. Arens, "Value of fluorescence endoscopy for the early diagnosis of laryngeal cancer and its precursor lesions," *Head Neck*, vol. 33, no. 7, pp. 941–948, Jul. 2011.

[12] T. P. Chang, F. Palazzo, N. Tolley, V. Constantinides, G. Z. Yang, and A. Darzi, "Vascularity assessment of parathyroid glands using confocal endomicroscopy: Towards an intraoperative imaging tool for real-time in situ viability assessment," *Eur. J. Surgical Oncol.*, vol. 40, p. S3, Oct. 2014.

[13] T. Vercauteren, A. Perchant, G. Malandain, X. Pennec, and N. Ayache, "Robust mosaicing with correction of motion distortions and tissue deformations for *in vivo* fibered microscopy," *Med Image Anal.*, vol. 10, no. 5, pp. 673–692, Oct. 2006.

[14] J. Mahé, T. Vercauteren, B. Rosa, and J. Dauguet, "A Viterbi approach to topology inference for large scale endomicroscopy video mosaicing," in *Proc. Int. Conf. Med. Image Comput. Comput.-Assist. Intervent.*, 2013, pp. 404–411.

[15] H. Wang, N. Zhang, and S. Zuo, "Low-cost and highly flexible intraoperative endomicroscopy system for cellular imaging," *Appl Opt.*, vol. 57, no. 7, pp. 1554–1561, Mar. 2018.

[16] S. Zuo, M. Hughes, and G. Yang, "Flexible robotic scanning device for intraoperative endomicroscopy in MIS," *IEEE/ASME Trans. Mechatronics*, vol. 22, no. 4, pp. 1728–1735, Aug. 2017.

[17] M. S. Erden, B. Rosa, N. Boularot, B. Gayet, G. Morel, and J. Szewczyk, "Conic-Spiraleur: A miniature distal scanner for confocal microlaparoscope," *IEEE/ASME Trans. Mechatronics*, vol. 19, no. 6, pp. 1786–1798, Dec. 2013.

[18] S. Zuoet, M. Hughes, C. Seneci, T. P. Chang, and G. Z. Yang,"Toward intraoperative breast endomicroscopy with a novel surface-scanning device," *IEEE Trans. Biomed. Eng.*, vol. 62, no. 12, pp. 2941–2952, Dec. 2015.

[19] S. Zuoet, M. Hughes, and G. Z. Yang, "Novel balloon surface scanning device for intraoperative breast endomicroscopy," *Ann. Biomed. Eng.*, vol. 44, no. 7, pp. 2313–2326, Jul. 2016.

[20] P. Giataganas, M. Hughes, C. J. Payne, P. Wisanuvej, B. Temelkuran, and G. Yang, "Intraoperative robotic-assisted large-area high-speed microscopic imaging and intervention," *IEEE Trans. Biomed. Eng.*, vol. 66, no. 1, pp. 208–216, Jan. 2019.

[21] R. C. Newton, D. Noonan, C. Payne, J. Andreyev, and A. Di Marco, "Probe tip contact force and bowel distension affect crypt morphology during confocal endomicroscopy," *Gut*, vol. 60, pp. A12–A13, Apr. 2011.

[22] Y. Ti and W. C. Lin, "Effects of probe contact pressure on *in vivo* optical spectroscopy," *Opt. Express*, vol. 16, no. 6, pp. 4250–4262, Mar. 2008.

[23] W. T. Lattet, T. P. Chang, A. Di Marco, P. Pratt, K.-W. Kwok, J. Clark, and G.-Z. Yang, "A hand-held instrument for *in vivo* probe-based confocal laser endomicroscopy during minimally invasive surgery," in *Proc. IEEE/RSJ Int. Conf. Intell. Robots Syst.*, Oct. 2012, pp. 1982–1987.
[24] W. T. Latt, R. C. Newton, M. Visentini-Scarzanella, C. J. Payne, D. P. Noonan, J. Shang, and G.-Z. Yang, "A hand-held instrument to maintain steady tissue contact during probe-based confocal laser endomicroscopy," *IEEE Trans. Biomed. Eng.*, vol. 58, no. 9, pp. 2694–2703, Sep. 2011.
[25] J. G. Bomers, E. B. Cornel, J. J. Fütterer, S. F. M. Jenniskens, H. E. Schaafsma, J. O. Barentsz, J. P. M. Sedelaar, C. A. Hulsbergen-van de Kaa, and J. A. Witjes, "MRI-guided focal laser ablation for prostate cancer followed by radical prostatectomy: Correlation of treatment effects with imaging," *World J. Urol.*, vol. 35, no. 5, pp. 703–711, May 2017.
[26] Y. Fan, Y. Sun, W. Chang, X. Zhang, J. Tang, L. Zhang, and H. Liao, "Bioluminescence imaging and two-photon microscopy guided laser ablation of GBM decreases tumor burden," *Theranostics*, vol. 8, no. 15, pp. 4072–4085, Jul. 2018.
[27] J. Heisterkamp, R. van Hillegersberg, P. E. Zondervan, and J. N. M. IJzermans, "Metabolic activity and DNA integrity in human hepatic metastases after interstitial laser coagulation (ILC)," *Lasers Surg. Med.*, vol. 28, no. 1, pp. 80–86, 2001.
[28] N. Bedard, T. Quang, K. Schmeler, R. Richards-Kortum, and T. S. Tkaczyk, "Real-time video mosaicing with a high-resolution microendoscope," *Biomed. Opt. Express*, vol. 3, no. 10, pp. 2428–2435, Oct. 2012.
[29] V. Becker, T. Vercauteren, C. H. von Weyhern, C. Prinz, R. M. Schmid, and A. Meining, "High-resolution miniprobe-based confocal microscopy in combination with video mosaicing (with video)," *Gastrointestinal Endoscopy*, vol. 66, no. 5, pp. 1001–1007, Nov. 2007.
[30] Z. Dai, R. Yang, F. Hang, J. Zhuang, Q. Lin, Z. Wang, and Y. Lao, "Neurosurgical craniotomy localization using interactive 3D lesion mapping for image-guided neurosurgery," *IEEE Access*, vol. 7, pp. 10606–10616, 2019.
[31] H. Liao, M. Tsuzuki, T. Mochizuki, E. Kobayashi, T. Chiba, and I. Sakuma, "Fast image mapping of endoscopic image mosaics with three-dimensional ultrasound image for intrauterine fetal surgery," *Minimally Invasive Therapy Allied Technol.*, vol. 18, no. 6, pp. 332–340, Dec. 2009.
[32] M. Zhou, X. Hao, A. Eslami, K. Huang, C. Cai, C. P. Lohmann, N. Navab, A. Knoll, and M. A. Nasseri, "6DOF needle pose estimation for robot-assisted vitreoretinal surgery," *IEEE Access*, vol. 7, pp. 63113–63122, 2019.
[33] B. Rosa, M. S. Erden, T. Vercauteren, B. Herman, J. Szewczyk, and G. Morel, "Building large mosaics of confocal edomicroscopic images using visual servoing," *IEEE Trans. Biomed. Eng.*, vol. 60, no. 4, pp. 1041–1049, Apr. 2012.
[34] G. Lu, J. V. Little, X. Wang, H. Zhang, M. R. Patel, C. C. Griffith, M. W. El-Deiry, A. Y. Chen, and B. Fei, "Detection of head and neck cancer in surgical specimens using quantitative hyperspectral imaging," *Clin. Cancer Res.*, vol. 23, no. 18, pp. 5426–5436, Sep. 2017.
[35] N. Zaidi, E. Bucak, P. Yazici, S. Soundararajan, A. Okoh, H. Yigitbas, C. Dural, and E. Berber, "The feasibility of indocyanine green fluorescence imaging for identifying and assessing the perfusion of parathyroid glands during total thyroidectomy," *J. Surg. Oncol.*, vol. 113, no. 7, pp. 775–778, Jun. 2016.

HAIBO WANG received the B.S. degree in naval architecture and ocean engineering from Harbin Engineering University, Harbin, China, in 2015. He is currently pursuing the Ph.D. degree with the School of Mechanical Engineering, Tianjin University, Tianjin, China.

His current research interests include medical robotics and instruments, and image-guided surgery.

ZHONGYUAN PING received the B.S. and master's degrees in mechanical design and automation from Northeast Agriculture University, Harbin, China, in 2015 and 2017, respectively. He is currently pursuing the Ph.D. degree with the School of Mechanical Engineering, Tianjin University, Tianjin, China.

His current research interests include medical robotics and instruments, and image processing.

YINGWEI FAN received the B.S. degree in biomedical engineering from the Kunming University of Science and Technology, Kunming, China, in 2012, the master's degree in biomedical engineering from Northeastern University, Shenyang, China, in 2014, and the Ph.D. degree from the Department of Biomedical Engineering, School of Medicine, Tsinghua University, Beijing, China, in 2018.

He is currently a Postdoctoral Researcher with the Beijing Institute of Radiation Medicine. His current research interests include minimally invasive theranostics, biomedical optics, optical coherence tomography, image-guided surgery, and laser medicine.

HONGXIANG KANG received the master's degree from the National University of Defense Technology, in 2005, and the Ph.D. degree from Tsinghua University, in 2009.

He is currently an Associate Professor with the Beijing Institute of Radiation Medicine. His current research interests include optical engineering, optical coherence tomography, biomedical optics, laser biological effect, and laser medicine. He is a member of the National Technical Committee on Light Radiation Safety and Laser Equipment, Standardization Administration of China. He is also a member of the Chinese Stereology Society. He also serves on the Editorial Advisory Board of the Laser Technology.

SIYANG ZUO received the M.Eng. and Ph.D. degrees in information science and technology from The University of Tokyo, Tokyo, Japan, in 2009 and 2013, respectively.

He is currently a Professor with the Key Laboratory of Mechanism Theory and Equipment Design of the Ministry of Education, School of Mechanical Engineering, Tianjin University, Tianjin, China. His current research interests include medical robotics and imaging techniques.